

Integrated DME/INS Alternative PNT System for RNP 1

Birendra Kujur, Samer Khanafseh, Boris Pervan, *TruNav LLC*
Valeriu Vitan, Gerhard Berz, *EUROCONTROL*
Okuary Osechas, *Zurich University of Applied Sciences*

BIOGRAPHY

Dr. Birendra Kujur serves as a Senior Research Associate in the Department of Mechanical and Aerospace Engineering at the Illinois Institute of Technology and as a Navigation Engineer at TruNav LLC. He earned both his M.S. and Ph.D. degrees from IIT, following a Bachelor of Science in Mechanical Engineering from Purdue University. His research is centered on advanced navigation technologies, with a particular emphasis on multi-sensor fusion and integrity monitoring. His current work explores the detection and mitigation of GNSS spoofing attacks, the development of robust anti-spoofing methodologies, and satellite fault diagnosis. His contributions aim to enhance the resilience and reliability of navigation systems in safety-critical applications.

Dr. Samer Khanafseh is currently a research associate professor at Illinois Institute of Technology (IIT), Chicago, and the principal of TruNav LLC. He received his MSc and PhD degrees in Aerospace Engineering from IIT in 2003 and 2008, respectively. Dr. Khanafseh has been involved in several aviation applications such as Autonomous Airborne Refueling (AAR) of unmanned air vehicles, autonomous shipboard landing for NUCAS and JPALS programs and Ground Based Augmentation System (GBAS). His research interests are focused on high accuracy and high integrity navigation algorithms, cycle ambiguity resolution, high integrity applications, fault monitoring and robust estimation techniques. He was the recipient of the 2011 Institute of Navigation Early Achievement Award for his outstanding contributions to the integrity of carrier phase navigation systems.

Dr. Boris Pervan is a Professor and Frank Gunsaulus Faculty Fellow in Mechanical and Aerospace Engineering at the Illinois Institute of Technology (IIT), where he conducts research on high integrity navigation systems. Prior to joining the faculty at IIT, he was a spacecraft mission analyst at Hughes Aircraft Company (now Boeing) and a postdoctoral research associate at Stanford University. Prof. Pervan received his B.S. from the University of Notre Dame, M.S. from the California Institute of Technology, and Ph.D. from Stanford University. He has received the Samuel M. Burka and Johannes Kepler Awards from the Institute of Navigation (ION), IIT Sigma Xi Excellence in University Research Award (twice), IIT University Excellence in Teaching Award, IEEE Aerospace and Electronic Systems Society M. Barry Carlton Award, RTCA William E. Jackson Award, Guggenheim Fellowship (Caltech), and the Albert J. Zahm Prize in Aeronautics (Notre Dame). He is a Fellow of the ION and former Editor-in-Chief of the ION journal NAVIGATION.

Valeriu Vitan is a senior expert in navigation infrastructure at EUROCONTROL, based in Brussels, Belgium. His work focuses on aviation navigation systems, particularly in the context of Performance-Based Navigation (PBN) and Alternate Positioning, Navigation, and Timing (A-PNT) strategies. He has contributed to research on Distance Measuring Equipment (DME) and its role as a terrestrial backup to satellite-based navigation systems like GNSS.

Gerhard Berz has a Bachelor's degree in avionics from Embry Riddle Aeronautical University and a Master's degree from the Ohio University Avionics Engineering Center. After professional experience at the US Naval Air Systems Command and skyguide, the Air Navigation Service Provider in Switzerland, he is now head of navigation at EUROCONTROL. As vice chair of the ICAO Navigation Systems Panel and chair of EUROCAE WG107, DME supporting PBN, he has developed a variety of system and global policy improvements in GNSS, interference mitigation and terrestrial navigation, including related radio spectrum issues.

Dr. Okuary Osechas is a researcher at Zurich University of Applied Sciences (ZHAW), in Switzerland. He holds a Ph.D. in Electrical Engineering from Tufts University. His work focuses on terrestrial navigation systems, GNSS resilience, and Performance-Based Navigation (PBN).

ABSTRACT

This paper proposes an alternative Position, Navigation, and Timing (APNT) system that integrates a tightly coupled Distance Measuring Equipment (DME)/Inertial Navigation System (INS) within a Kalman Filter (KF) architecture. This configuration satisfies the Required Navigation Performance (RNP) 1 criteria for straight-and-level flight across European airspace. While RNP has traditionally been supported by Global Navigation Satellite Systems (GNSS), its expansion into airspaces with tighter

requirements continues globally (RTCA SC-227 (2025a), RTCA SC-227 (2025b)).

RNP’s standardized framework and benefits—such as increased airspace capacity and precise route guidance—make it an appealing candidate for continued adoption. However, the growing incidence of GNSS jamming and spoofing (Kerns et al. (2014), Kujur et al. (2024)) threatens its reliability. Currently, no standards exist for complete GNSS failure scenarios. As a result, aviation stakeholders are actively exploring resilient APNT solutions as potential GNSS backups (Berz et al. (2013), Vitan et al. (2015), Osechas et al. (2022)). Among terrestrial navigation aids, DME presents a promising foundation for APNT architectures due to its legacy infrastructure and operational robustness (Berz and Saini (2022), Lo et al. (2013), Lo et al. (2013), Lo and Enge (2012b), Vitan and Theißen (2016)).

The performance of the multi-DME KF system is first evaluated in a representative scenario. Subsequently, the integrated DME/INS KF system is assessed, including its inertial coasting capability during complete DME signal outages. Results demonstrate that this architecture can achieve position errors with a standard deviation of less than 50 meters. To enhance system integrity, solution separation–based fault detection, identification, and exclusion (FDE) is implemented by running a bank of KFs (Gunning et al. (2019); Tanil et al. (2019)). Protection level results are presented for the integrated DME/INS system, indicating its potential to satisfy RNP 1 integrity requirements. The analysis also considers various grades of Inertial Measurement Units (IMUs) to evaluate the system’s suitability for general aviation.

I. INTRODUCTION

1. RNP

Required Navigation Performance (RNP) is a navigation specification that enables aircraft to follow a defined trajectory while ensuring that lateral deviations from the centerline do not exceed the Total System Error (TSE) allowance. RNP designations typically include a numerical value—expressed in nautical miles (NM)—that represents the allowable TSE; for example, RNP 1 and RNP 0.3 are commonly employed service types. The TSE is frequently referred to as “the RNP number”. The RNP framework mandates that users continuously monitor navigation performance to ensure compliance with the specified standard.

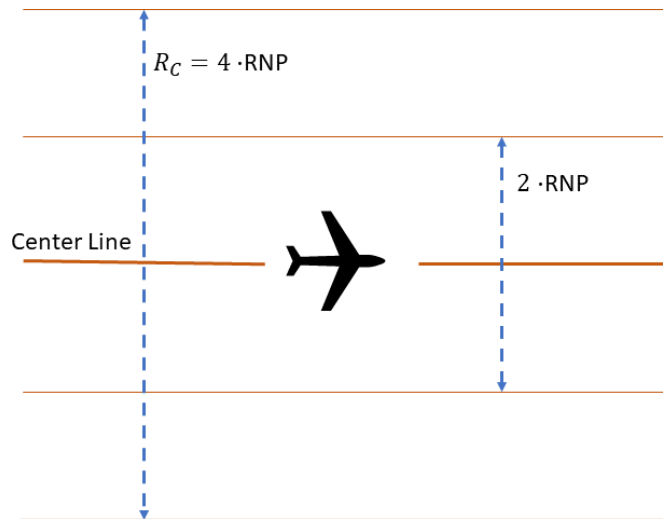


Figure 1: RNP is designed to keep an aircraft inside a corridor defined around a center line. TSE shall not exceed twice the RNP value with a probability of 95% or better, while R_C shall be exceeded no more than $6.3 \times 10^{-5}/h$.

The Total System Error (TSE) comprises three components: Navigation System Error (NSE), Flight Technical Error (FTE), and Path Definition Error (PDE) (International Civil Aviation Organization (2023)). The PDE, a legacy term, is typically modeled as zero in current applications. The TSE is calculated as the root-sum-square (RSS) of these components:

$$TSE^2 = NSE^2 + FTE^2 + PDE^2, \quad (1)$$

where, the NSE is defined as the standard deviation of the lateral component of the position estimate. It reflects the uncertainty in the estimated aircraft position. The FTE, by contrast, captures deviations due to the aircraft’s control performance—accounting for its limited ability to perfectly track the intended path in the presence of disturbances and dynamic control constraints.

In addition to defining the TSE as the primary performance metric, relevant standards (International Civil Aviation Organization (2023), RTCA SC-227 (2025a), RTCA SC-227 (2015)) introduce a *Containment Methodology* to ensure aircraft remain within a defined containment area proportional to the TSE. A loss of integrity is said to occur if the position error exceeds a critical threshold without timely alerting the operator. The containment radius, R_C , is specified in (RTCA SC-227 (2015)) as twice the TSE, which corresponds to a four-sigma alert limit and an integrity risk of 6.3×10^{-5} . This definition aligns with the alert limit requirement for RNP compliance.

To satisfy the RNP 1 requirement, the Total System Error (TSE) must remain within 2 nautical miles with a probability of 95% or greater, while the containment radius, R_C , must be exceeded no more than 6.3×10^{-5} occurrences per hour. Accordingly, the proposed Alternative Position, Navigation, and Timing (APNT) system must meet both the accuracy criterion and incorporate an integrity monitoring mechanism that generates protection levels conforming to containment standards.

While RNP is currently supported by Global Navigation Satellite Systems (GNSS), the increasing vulnerability of GNSS to jamming and spoofing threats has prompted renewed interest in Distance Measuring Equipment (DME) as a resilient alternative for meeting RNP requirements in safety-critical airspace operations.

2. DME

DME is a two-way ranging system where an aircraft sends an interrogation to a DME station and receives a reply signal, which is used to determine the aircraft's location relative to the DME station (Kelly and Cusick (1986)). DME already has existing infrastructure on the ground and on-board equipment and antennas on most aircraft. The gap that exists with DME systems is the performance specifications with regard to accuracy, integrity, and continuity requirements to meet standards such as RNP. Additionally, there are few current solutions that address the ability of DME systems to detect and recover from faults or security threats (Zampieri et al. (2021)). Prior work has been done to develop enhanced DME systems which have better performance than current capabilities but require changes in infrastructure and aircraft avionics (Kim (2022), Lo et al. (2020), Lo and Enge (2012a), Lo et al. (2015)).

It has been shown previously that the integration of DME with auxiliary sensors such as Inertial Navigation System (INS) in sequential filters can significantly improve performance (Gebre-Egziabher et al. (2000), Latham and Richards (1977), Strecha et al. (2018)). Current implementations of integrated DME/INS sensors are proprietary, owned by avionics manufacturers. No standard performance models exist, and airspace planners cannot make assumptions about the navigation performance of aircraft during GNSS outages. Given that these GNSS outages are, effectively, permanent in some parts of the world, integrated DME/INS is a compelling candidate for providing an alternative capability. The ability to implement fault detection, identification, and exclusion (FDE) on DME-based navigation is a game changer that can finally deliver the necessary integrity for RNP services and all the automation and safety benefits it brings to the airspace. It is a necessary step in the standardization of integrated DME/INS as a viable alternative to GNSS on a wide scale. Appendix .B details the integrated tightly-coupled DME/INS Kalman filter (KF) model.

DME performance by itself has been recognized to be limited by multipath errors and a few solutions have been proposed (Gordo et al. (2019), Lo et al. (2014), Osechas et al. (2023), Vitan et al. (2022), Osechas et al. (2020), Pelgrum and Li (2015), Tripathi and Caizzone (2024)). We aim to utilize the advantage of INS for an integrated DME/INS system that can meet aviation standard requirements for accuracy. Additionally, we develop a fault detection, identification, and exclusion method for excessive multipath errors for the DME/INS system to meet the integrity and continuity requirements. We utilize the GNSS/INS integrated system standard (RTCA SC-159 (2020)) as a reference for developing the DME/INS system. In this paper we will also analyze the INS-only coasting behavior of the proposed fusion algorithm. DME coverage is, in general, patchy. Over Europe, many gaps in coverage exist, especially at lower altitudes and on final approach. Adequate inertial integration will extend the coverage of DME to areas with relatively poor network coverage and to areas near final approaches, where measurement deprivation can lead to large, out-of-tolerance errors can become hazardous if not monitored.

Section II describes the architectures of both the multi-DME Kalman Filter (KF) system and the integrated DME/INS KF system. Section III presents performance results for each configuration, including scenarios involving complete DME signal outages. Section IV details the implementation of the DME/INS fault detection, identification, and exclusion (FDE) method and its associated results. Section V concludes the paper, with an appendix provided for supplementary material.

II. MULTI-DME AND DME/INS SEQUENTIAL ESTIMATION

DME measurements can be used at each time step to determine a position solution through snapshot estimation techniques such as Least Squares. When a sequence of such measurements is available, they can also be processed in batch mode to enhance position accuracy. Alternatively, DME measurements may be incorporated into a recursive filter—such as a Kalman Filter (KF)—either independently using a dynamic model or in conjunction with additional sensors such as an Inertial Measurement Unit (IMU). In this paper, the former approach is referred to as the multi-DME KF, while the latter integrated configuration is

termed the DME/INS tightly-coupled KF. In this context, tightly coupled denotes a KF architecture in which DME and IMU measurements are fused directly within a unified estimation framework.

KF requires a process model, which predicts state estimates and state error covariances. These predictions, referred to as *a priori* state estimates and error covariances, serve as the basis for further updates. Typically, these estimates are refined once measurements from one or more sensors are received. Based on the new sensor data and its measurement quality—specified by the measurement error covariance—both the state estimate and error covariance are updated in an optimal manner. Here, “optimal” refers to minimizing the state estimate error. The resulting updates are known as *a posteriori* state estimates and error covariances. The process of leveraging a prior state estimate and updating it with a relatively small correction after receiving new sensor measurements helps smooth the state estimates.

In vehicle navigation, the process model represents the dynamic behavior of the vehicle, which may or may not incorporate sensor measurements, such as those from an IMU. The process model update rate is typically faster than the measurement update rate. In typical navigation applications, the estimated states include the vehicle’s position, velocity, and attitude, as well as error states associated with process or measurement models that must be compensated.

Even though PBN services only require estimating a position in two dimensions, usually latitude and longitude, the KF implementation will require a full three-dimensional setup. The navigation architecture considered in this work is a tightly-coupled integration. The dynamics of the system is represented with the process model,

$$\mathbf{x}_{k+1} = \Phi_k \mathbf{x}_k + \Gamma_{w_k} \mathbf{w}_k, \tag{2}$$

where \mathbf{x}_k is the unknown state vector, Φ_k is the state transition matrix, Γ_{w_k} is the process noise model matrix, and \mathbf{w}_k is the additive white process noise with a respective covariance matrix \mathbf{Q}_k . The measurement model is

$$\mathbf{z}_k = \mathbf{H}_k \mathbf{x}_k + \mathbf{v}_k, \tag{3}$$

where \mathbf{H}_k is the observation matrix and \mathbf{v}_k is the measurement noise with a respective covariance matrix \mathbf{V}_k . The appendices .A and .B outlines the architectures of both the multi-DME and the integrated DME/INS KF.



Figure 2: Aircraft trajectory for KF simulation.

1. Multi-DME KF

The scenario for this evaluation is a straight level flight (SLF) of an aircraft starting from Berlin Brandenburg Airport (52.3650° N, 13.5010° E) illustrated in Figure 2. An East-North-Up reference navigation frame is fixed at this location. The aircraft cruises at a speed of 200 m/s (approximately 400 knots) along the eastward direction at an altitude of 18,000 ft (5486 m).

Table 1: Example process noise specifications.

Parameter	Value	Units
Acceleration noise std. dev. in East direction (σ_{a_x})	1	m/s^2
Acceleration noise std. dev. in North direction (σ_{a_y})	1	m/s^2
Acceleration noise std. dev. in Up direction (σ_{a_z})	1	m/s^2

Table 2: Barometric altimeter noise specifications.

Parameter	Value	Units
Thermal noise standard deviation (σ_{baro})	60	m
Bias standard deviation ($\sigma_{baro\ bias}$)	10	m

Table 3: DME modeling assumptions.

Parameter	Value	Units
DME minimum elevation	0.76	degrees
DME maximum elevation	40	degrees
DME measurement frequency	5	Hz
DME measurement noise standard deviation (σ_{dme})	180	m

This SLF trajectory is commonly used for validating GNSS/INS integrated systems. We will reference the MOPS for these systems in developing similar criteria for a DME/INS system later (RTCA SC-159 (2020)). Alongside multiple DME measurements, the aircraft utilizes a barometric altimeter to determine its altitude, with noise values selected based on (RTCA-SC-227 (2014)) (Table 2). The altitude measurements are used to transform DME slant range measurements into horizontal ranges.

The aircraft is assumed to experience small random accelerations that introduce perturbations in position and velocity states along the nominal trajectory. These example random accelerations are modeled as zero-mean white Gaussian noise, with specifications detailed in Table 1. For this evaluation, we assume a flat terrain, assuming that the effect of signal occlusions due to topography have a negligible effect on algorithm design.

The process update frequency is set at 20 Hz, while measurement updates for both the barometric altimeter and all in-view DME are set at 5 Hz. The DME measurement noise standard deviation is conservatively modeled as $\sigma_{dme} = 180\text{ m}$ and the maximum elevation angle is set to 40° , as per (EUROCAE WG-107 (1986)), with other specifications listed in Table 3. Since at least six DME measurements are consistently available for this trajectory, we select $N = 6$ DME measurements available for all time during this simulation. The DME measurements are modeled as true range with additive white noise.

Figure 3 illustrates an aircraft at position (x_a, y_a, z_a) utilizing multiple DME stations for slant range measurements (ρ_{dme}) and a barometric altimeter to determine altitude. The barometric altimeter is modelled as true altitude with additive bias and white noise with noise specification in Table 2.

Here, we assume that the barometric altimeter measurement (h_{baro}) provides aircraft altitude relative to the geodetic datum defined by the World Geodetic System (WGS84). The locations of both the aircraft and DME stations are expressed in the navigation frame. The angles β_{dme} represent the elevation angles of DME stations relative to the aircraft. The barometric altimeter measurements are used to convert DME slant range measurements into horizontal ranges as illustrated in Figure 4. The angles θ_{dme} denote the orientation of the DME horizontal ranges relative to the navigation frame's x-axis (East direction).

Dynamic modeling of aircraft motion within a KF framework is generally more feasible during SLF segments, where the dynamics are relatively benign. In contrast, more complex flight phases—such as climbs, descents, or turns—often require

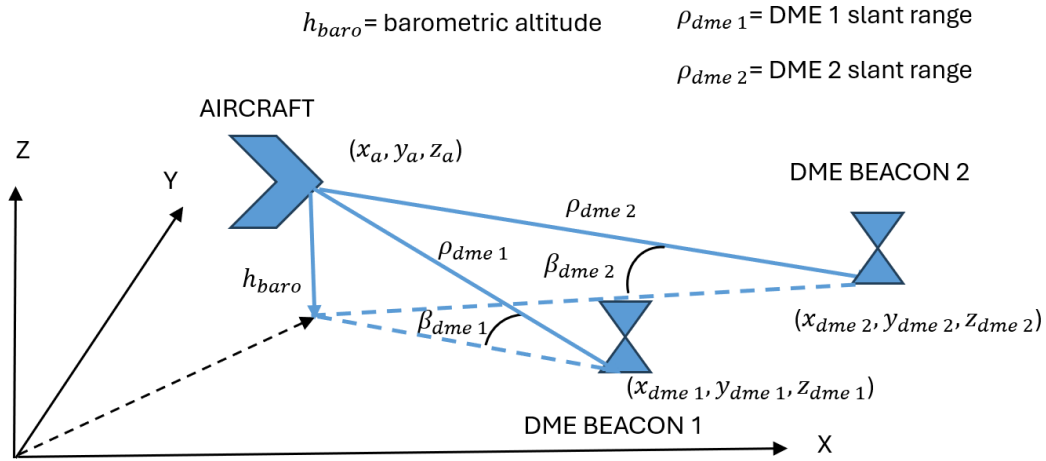


Figure 3: Illustration of multiple DME three-dimensional slant range measurements.

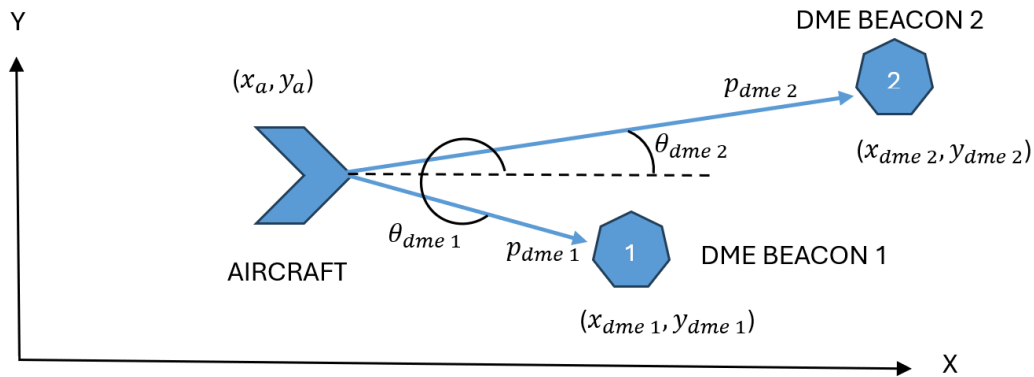


Figure 4: Illustration of multiple DME horizontal range measurements.

auxiliary sensing capabilities. In such cases, an INS is better suited to capturing the nuanced dynamic behavior. The following subsection presents a tightly coupled DME/INS KF system, a configuration more commonly adopted in practical applications for its robustness and accuracy across varying flight conditions.

2. DME/INS KF

The INS determines position, velocity, and orientation by processing three-dimensional accelerometer and gyroscope measurements from an Inertial Measurement Unit (IMU). Accelerometers provide linear acceleration, while gyroscopes measure body angular rates. These quantities are integrated to estimate the system's kinematic states—namely, position, velocity, and attitude. However, the IMU measurements are subject to various error sources, including white noise, constant bias, and time-varying bias. As these errors propagate through integration, they accumulate over time, resulting in drift in the estimated navigation states.

To mitigate integration drift, an INS is typically augmented by external aiding sensors such as GNSS, odometers, or laser-based systems. Conversely, INS enhances these aiding sources by providing smooth continuity in the navigation solution, particularly during temporary aiding sensor outages. In the context of a DME/INS integrated system, the INS can also serve as an auxiliary monitor, supporting anomaly detection in DME-derived measurements. Furthermore, redundancy from multiple DME ground stations enhances the system's ability to identify and reject faulty measurements, thereby improving overall fault detection and exclusion (FDE) performance.

For the DME/INS integration, a linearized INS mechanization is employed to represent the vehicle dynamics within the Kalman

Filter KF framework. This formulation serves as the process model, with associated uncertainties characterized by a process noise covariance matrix. The measurement model remains consistent with that used in the multi-DME configuration and incorporates barometric altimeter readings.

The evaluation scenario is identical to that described in the preceding subsection; however, the aircraft dynamics are now modeled using measurements from an IMU. Specifications for the navigation-grade and tactical-grade IMUs considered in this study are provided in Appendix .D, while the detailed formulation of the proposed DME/INS KF model is outlined in Appendix .B. A flat terrain assumption is applied throughout the scenario, as in the previous case.

The IMU provides process updates at a frequency of 20 Hz, while measurement updates from the barometric altimeter and all in-view DME stations are incorporated at 5 Hz. The DME modeling specifications used in the simulation are summarized in Table 3. For this evaluation, the best $N = 6$ DME measurements available at each epoch are selected to ensure optimal positioning performance.

III. RESULTS

1. Multi-DME KF results

The fault-free results for the three-dimensional position estimate error and covariances for the aforementioned trajectory, using the multi-DME KF system, are presented in Figures 5, 6, and 7. The position error and covariance results were generated for two different DME station selection algorithms. The first algorithm selects the N DME ground transponders nearest to the aircraft. The second algorithm searches for the optimal subset of N visible DME stations (every 100 seconds).

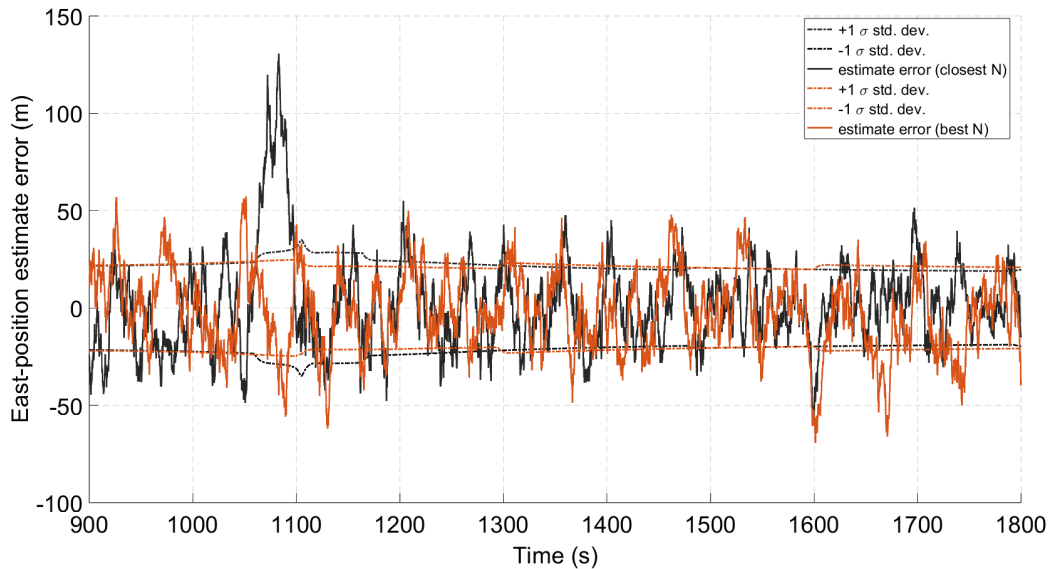


Figure 5: East position estimate error and covariance for closest and best 6 DME.

The total simulation duration was 30 minutes, with results illustrated after the first 15 minutes due to KF convergence. The results show that leveraging the time-smoothing and filtering properties of the KF significantly reduces position error covariance, compared to a standard least-squares snapshot positioning approach. Additionally, the process noise model and its associated covariance contribute to tighter position error covariances. If the process noise were significantly higher than the DME measurement noise, the position error covariance would depend solely on the measurement noise covariance and may approach the performance of the snapshot approach. The results indicate that selecting the best N in-view DME stations consistently provides better covariance performance than choosing the closest N . While the difference between these two approaches may seem marginal, it becomes notably significant during geometry degradation, as observed in Figure 5. In such scenarios, the best N configuration provides superior performance.

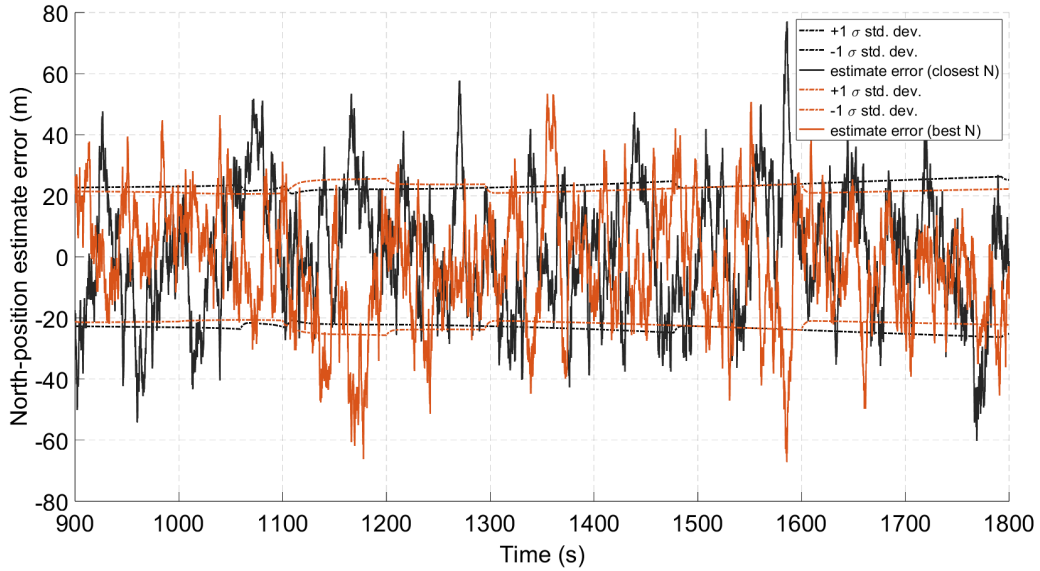


Figure 6: North position estimate error and covariance for closest and best 6 DME.

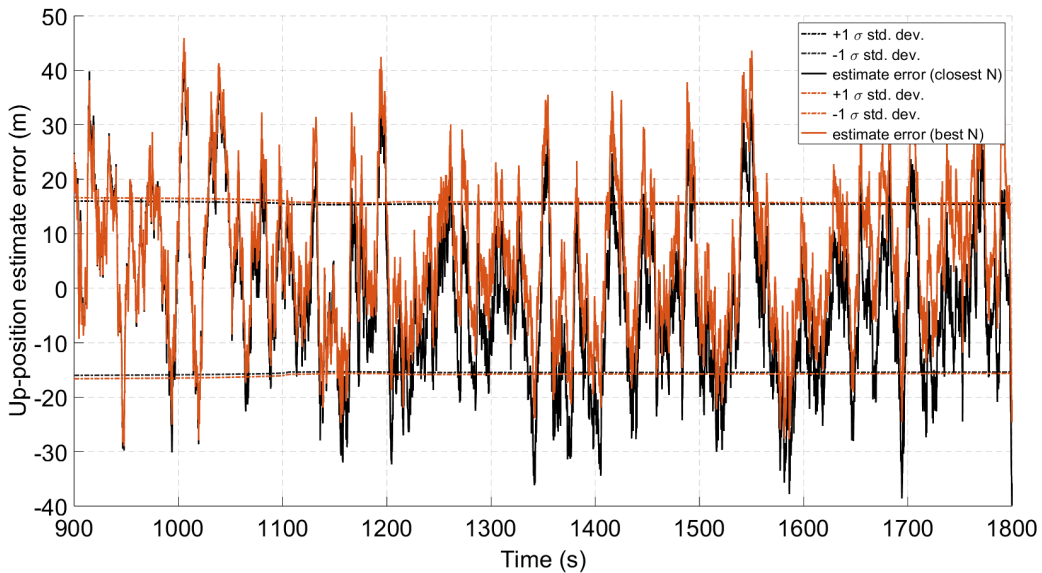


Figure 7: Vertical position estimate error and covariance for closest and best 6 DME.

2. DME/INS KF results

The position estimate and covariance results for the tightly coupled DME/INS KF system—using both tactical-grade and navigation-grade IMUs—are presented in Figures 8, 9, and 10. For this evaluation, the best $N = 6$ DME measurements available at each epoch are selected. These selections are updated every 100 seconds, leading to subtle changes in the covariance results that reflect the evolving DME geometry and measurement quality.

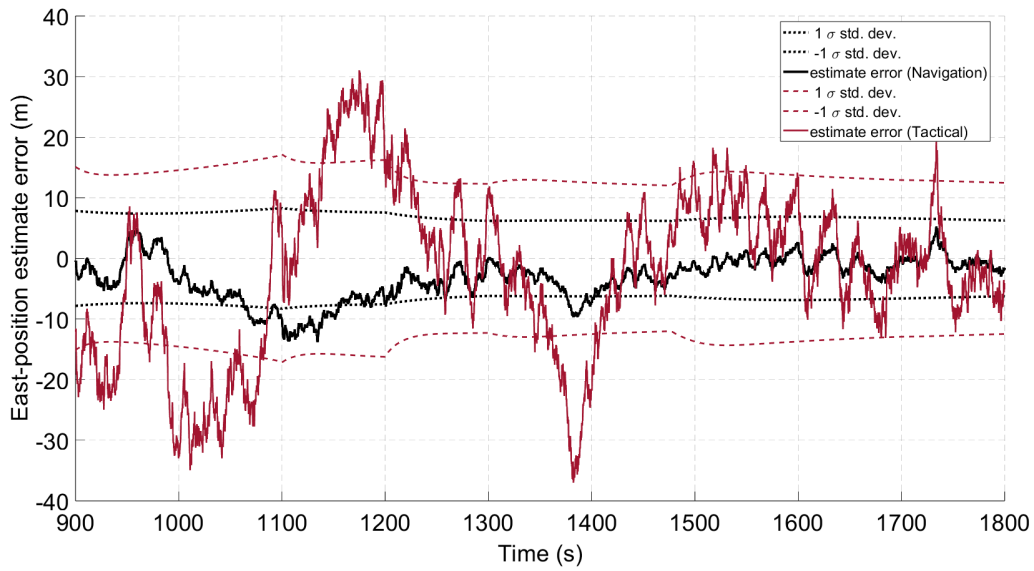


Figure 8: Illustration of DME/INS East position estimate error and covariance for tactical and navigation grade IMU.

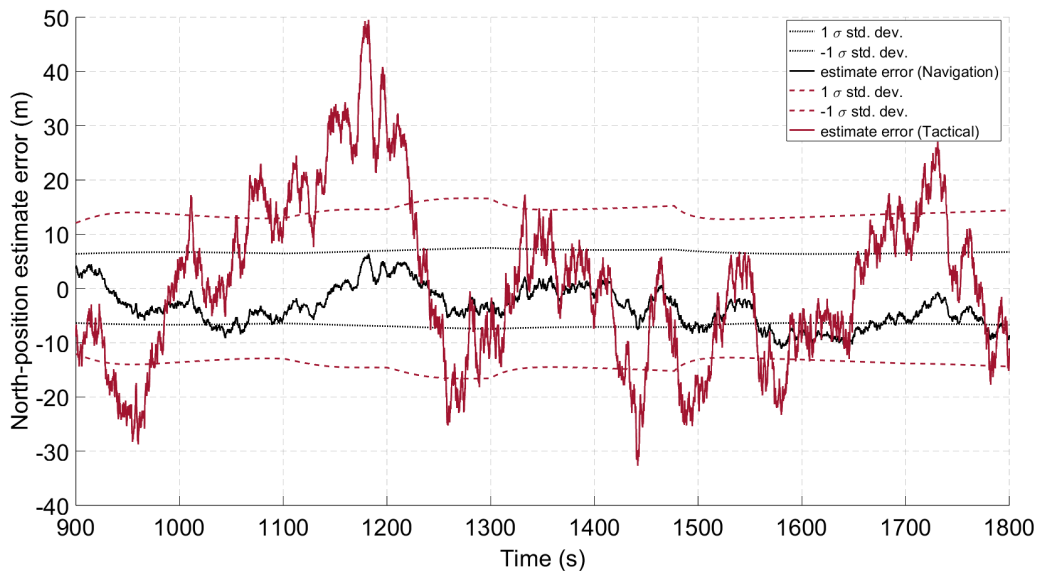


Figure 9: Illustration of DME/INS North position estimate error and covariance for tactical and navigation grade IMU.

The horizontal position error standard deviation is observed to be less than 30 m with a tactical-grade IMU and under 15 m with a navigation-grade IMU. These covariance results indicate that the RNP 1 accuracy requirement—defined as a two-sigma horizontal error within 2 nautical miles—can be readily satisfied using either IMU class. However, it is important to recognize that these findings reflect a best-case scenario based on idealized assumptions, including flat terrain and straight-and-level flight. Real-world operational conditions are likely to introduce additional sources of error that may degrade overall positioning performance.

The improvement in position estimate error covariance resulting from inertial smoothing, relative to the DME-only KF, is illustrated in Appendix .C. For the DME-only KF, the process noise standard deviation was set to $0.6g$ ($6 m/s^2$).

The results presented thus far are based on a single trajectory and, therefore, are not broadly representative of coverage or performance across the entirety of European airspace. To address this limitation, a map-based performance evaluation is

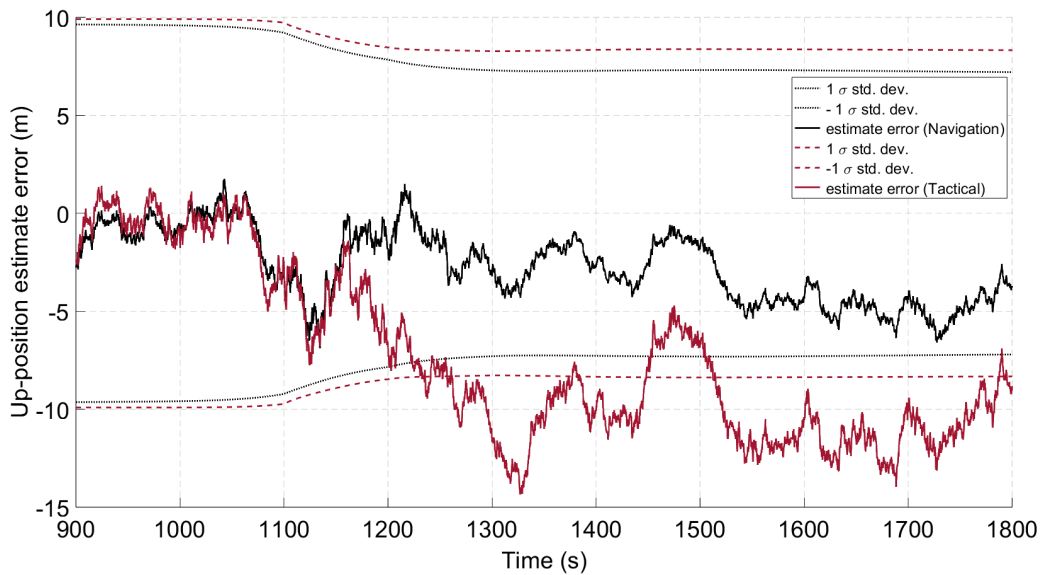


Figure 10: Illustration of DME/INS Up position estimate error and covariance for tactical and navigation grade IMU.

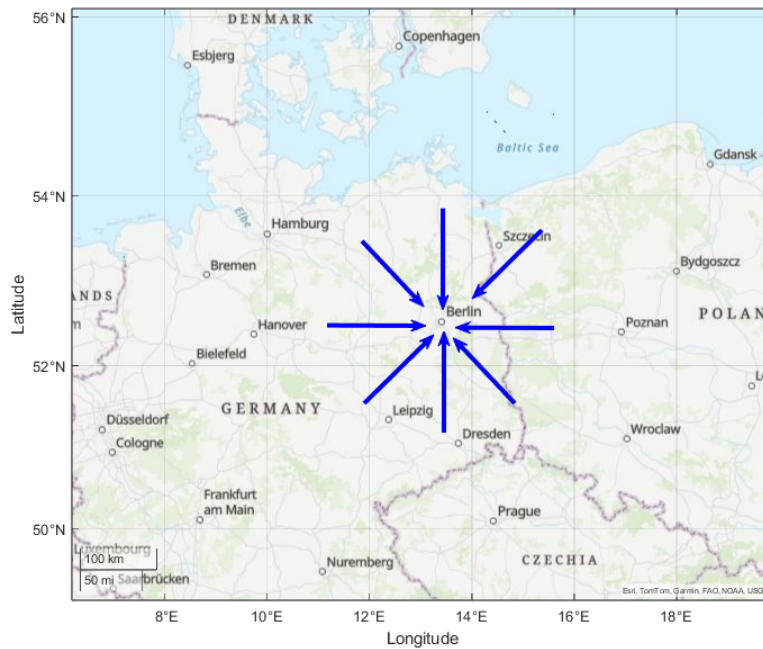


Figure 11: Illustration of flight trajectory scenario for map-based covariance evaluation.

conducted by simulating SLF trajectories directed toward each grid point at varying angular increments. At each grid location, the worst-case covariance is computed to assess the spatial variation in achievable positioning performance. This evaluation spans the full extent of EU airspace and offers a more comprehensive view of system capability under idealized conditions. It is important to emphasize that this analysis assumes SLF trajectories and does not account for more dynamic flight profiles; nevertheless, it represents a meaningful step toward robust, region-wide performance assessment.

Figure 11 illustrates a scenario in which flight trajectories are generated from various angles towards a single evaluation point. Figures 12 and 13 present the maximum horizontal standard deviation results at different evaluation grid points for navigation-grade and tactical-grade IMUs, respectively. Grid points where any trajectory lacked at least two available DME measurements

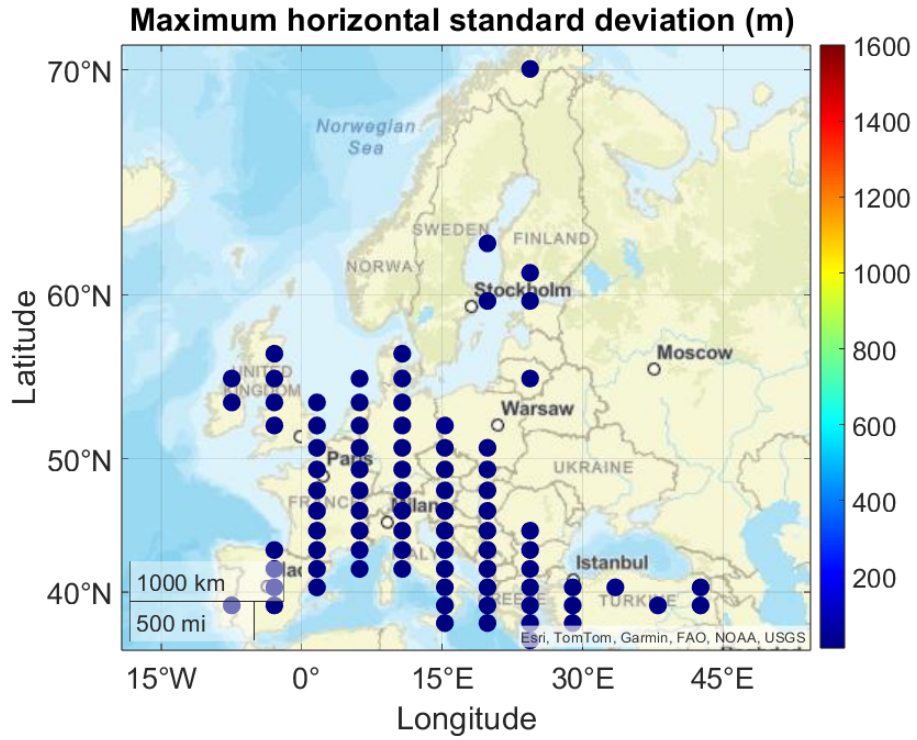


Figure 12: Maximum horizontal position standard deviation (meters) using navigation grade IMU.

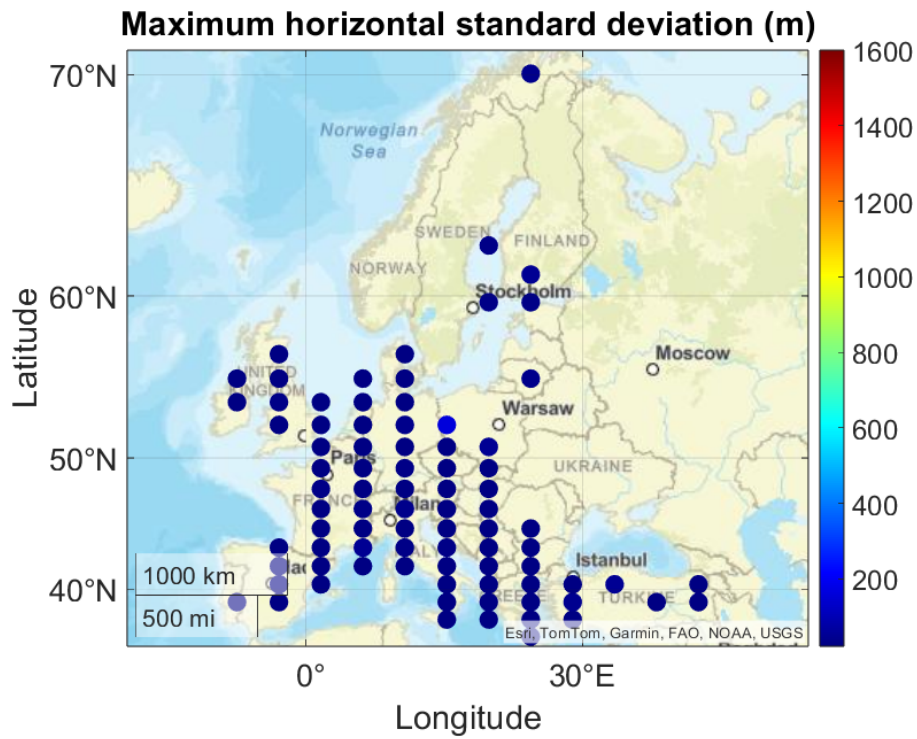


Figure 13: Maximum horizontal position standard deviation (meters) using tactical grade IMU.

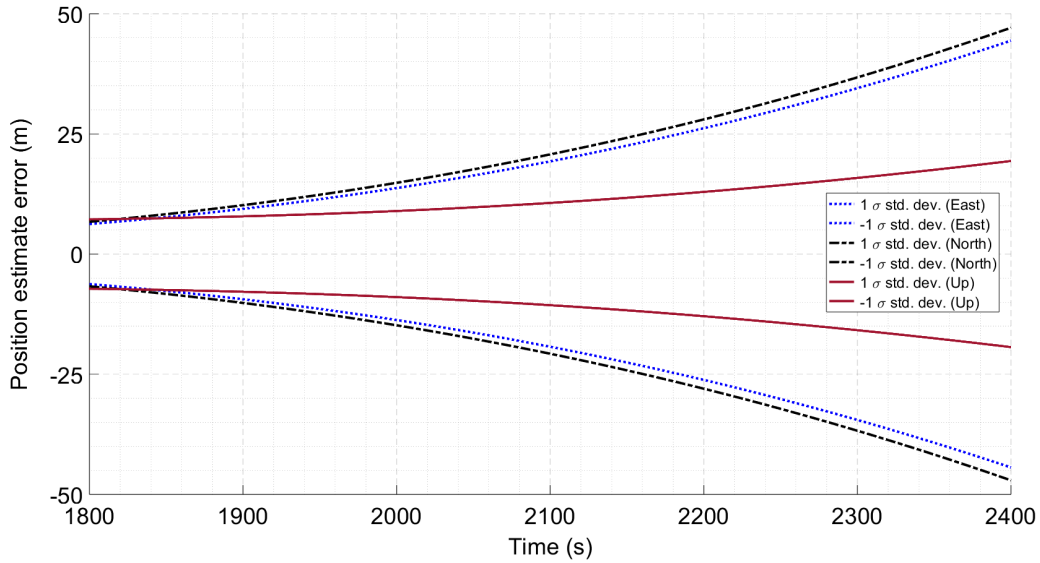


Figure 14: INS-only position estimate error covariance for navigation grade IMU.

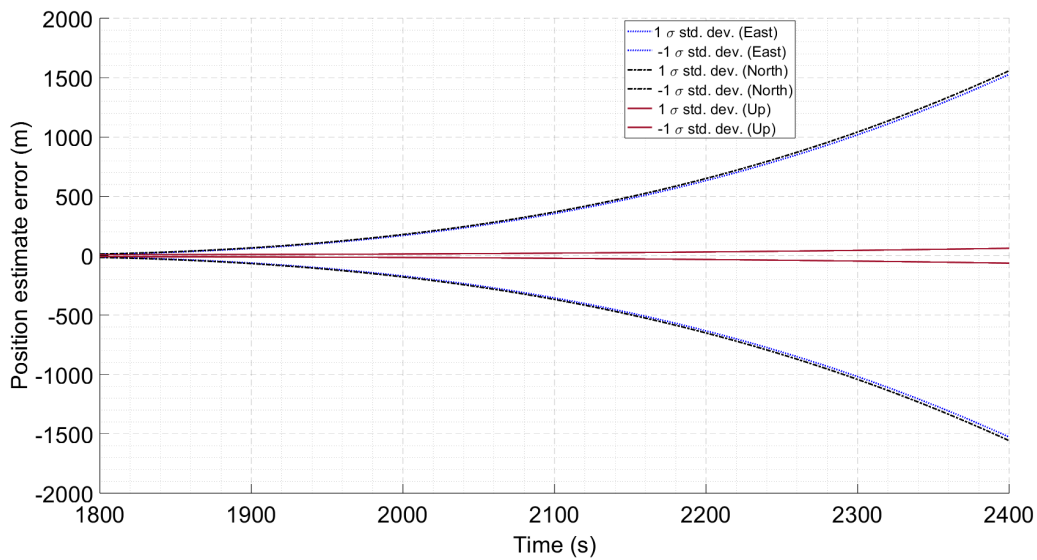


Figure 15: INS-only position estimate error covariance for tactical grade IMU.

were excluded from consideration, resulting in sparse evaluation results. The low variability in horizontal standard deviation across the map represents a promising outcome in support of DME/INS utilization for RNP 1 applications.

3. DME Outages

In the event of a complete DME outage, the aircraft relies on an INS-only solution to maintain its trajectory. A simulation is conducted in which the DME outage occurs after 30 minutes of SLF, with barometric altimeter measurements also excluded during the subsequent pure INS coasting phase. Figures 14 and 15 illustrate the resulting position errors and covariance estimates for navigation-grade and tactical-grade IMUs, respectively, over a 600-second interval. The pronounced difference between horizontal and vertical performance in tactical-grade INS is primarily due to the influence of gyro bias, which—under constant velocity conditions—affects only the horizontal navigation channels.

The results indicate that the navigation-grade IMU enables the aircraft to maintain compliance with RNP 1 accuracy requirements for a longer duration compared to the tactical-grade IMU. Specifically, while the tactical-grade IMU exceeds the RNP 1 threshold

after approximately five minutes, the navigation-grade IMU sustains acceptable accuracy for up to ten minutes, despite the accumulating drift characteristic of an unaided INS solution.

IV. DME FAULT DETECTION, IDENTIFICATION AND EXCLUSION (FDE)

1. FDE Methodology

DME measurements are susceptible to unintentional faults arising from either hardware malfunctions or environmental influences. This study focuses primarily on faults caused by environmental conditions, particularly those induced by excessive multipath. The preliminary DME measurement model adopted here assumes a true range corrupted by additive white Gaussian noise (WGN). However, under multipath conditions, the DME measurements are subject to biases or slowly varying trends (ramps), thereby deviating from nominal assumptions.

This work considers a single DME fault scenario. Fault detection and exclusion FDE within a recursive filter such as a KF presents additional complexity, as measurement faults become embedded in the filter's state history over time, making retrospective exclusion ineffective. Consequently, it is not sufficient to merely detect and discard a faulty measurement upon identification

To address this, a practical and scalable FDE approach for KF-based systems involves maintaining a bank of parallel Kalman subset filters, each corresponding to a specific fault hypothesis. For instance, given N DME measurements, the first fault hypothesis assumes that DME 1 is faulty. A corresponding subset filter—termed Subset Filter 1—is then run in parallel to the main KF but excludes DME 1 from its update set. Upon detection and confirmation of the fault in DME 1, the system transitions to Subset Filter 1, thereby removing the impact of the faulty measurement from subsequent estimation steps.

For detection, the solution-separation method is typically favored, as it does not assume a specific fault profile and instead evaluates faults directly in the position domain. In this method, the test statistic is defined as the difference in position solutions between the full-set KF and the corresponding subset filters. Under a single-fault hypothesis, where the i^{th} DME is suspected to be faulty, a full-set KF—denoted by superscript (0) —and subset filters—denoted by (i) —are employed. For example, let $\hat{x}^{(0)}$ and $\hat{x}^{(i)}$, represent the East position estimate from the full-set and i^{th} subset filter, respectively. The test statistic corresponding to the i^{th} fault hypothesis given by (Gunning et al. (2018))

$$q_{ss}^{(i)} = \hat{x}^{(0)} - \hat{x}^{(i)}. \quad (4)$$

The test statistic is normally distributed, with its covariance given by

$$\sigma_{ss}^{(i)2} = \sigma^{(i)2} - \sigma^{(0)2}, \quad (5)$$

where $\sigma^{(0)2}$ and $\sigma^{(i)2}$ represent the example East (x) position error variance obtained from full-set and subset KF, respectively.

If P_{FA} denotes the total horizontal false alarm probability requirement, the threshold can be determined using the inverse cumulative distribution function (CDF) of the normal distribution as follows:

$$T_i = Q^{-1}\left(\frac{\alpha_i P_{FA}}{2}\right) \sigma_{ss}^{(i)} \quad (6)$$

where Q denotes the complement of the normal CDF, and Q^{-1} its inverse. $\sigma_{ss}^{(i)}$ represents the standard deviation of the solution separation under nominal conditions, and α_i is the portion of P_{FA} allocated to the i^{th} hypothesis. The total allocation across all hypotheses must not exceed one.

A key advantage of the solution-separation method is its ability to evaluate protection levels in real time. The horizontal protection level (HPL) defines the radius of a horizontal circle centered on the aircraft's indicated position that, with a specified probability, encloses the true position. To satisfy the RNP 1 containment and integrity requirements, the HPL must remain below the containment radius R_c with a probability less than the allowable integrity risk. The maximum protection level under N fault hypotheses can be conservatively assessed using the formulation in (Gunning et al. (2018)):

$$PL_{max} = \max\left(T_i + Q^{-1}\left(\frac{\psi_i}{360} \frac{P_{HMI}}{2P(H_i)}\right) \sigma^{(i)}\right) \quad (7)$$

where P_{HMI} denotes the total integrity risk allocation, while ψ_i represents the portion of P_{HMI} assigned to the i^{th} hypothesis per hour, assuming a 10-second time-to-alert (TTA). The term $\sigma^{(i)}$ is the standard deviation of the position estimation error for

subset filter i , $P(H_i)$ is the probability of fault hypothesis i , and T_i is the corresponding threshold. The maximum horizontal protection level is expressed as

$$HPL_{max} = \sqrt{PL_{E_{max}}^2 + PL_{N_{max}}^2} \quad (8)$$

where Equation (7) is evaluated to obtain $PL_{E_{max}}$ and $PL_{N_{max}}$ for East and North directions, respectively.

Enhanced position error covariances enable tighter protection levels. Moreover, thanks to KF smoothing, these protection levels remain continuous and resilient, avoiding degradation in response to abrupt changes in DME geometry.

2. FDE Results

The use of RNP will influence certain decisions on bounding, or containing, the navigation error. In particular, the following quantities introduced in the previous subsection:

1. The probability of Hazardously Misleading Information P_{HMI} is 10^{-6} ;
2. The probability of false alarm P_{FA} is 10^{-5} ;
3. The prior probability of fault on i^{th} measurement $P(H_i)$.

Committing to hard-and-fast numbers for $P(H_i)$ will require extensive analysis of the problem, presumably by a committee of experts. For the time being, we assume $P(H_i) = 10^{-3}$. The false alarm and integrity risk allocations are uniformly distributed across all fault hypotheses, with $\alpha_i = 1/N$ and $\psi_i = 1/N$, where N denotes the number of DME in view.

Figure 16 illustrates the maximum HPL evaluated over the final 100 seconds of the trajectory. The results, computed using Equation (8), are presented for both tactical- and navigation-grade IMUs. They offer an encouraging indication that the integrity requirements for RNP 1 can be satisfied under a single DME fault hypothesis.

The example SLF trajectory demonstrates that the accuracy and integrity risk requirements for RNP 1 can be satisfied. However, this assessment relies on several optimistic assumptions, including predefined fault modes, fault probabilities, flat terrain, and consistent availability of DME measurements—rendering it a best-case scenario. A more rigorous evaluation is necessary to determine whether a DME/INS system can reliably meet RNP 1 requirements across EU airspace. Nevertheless, this work establishes a foundational framework upon which further research can build.

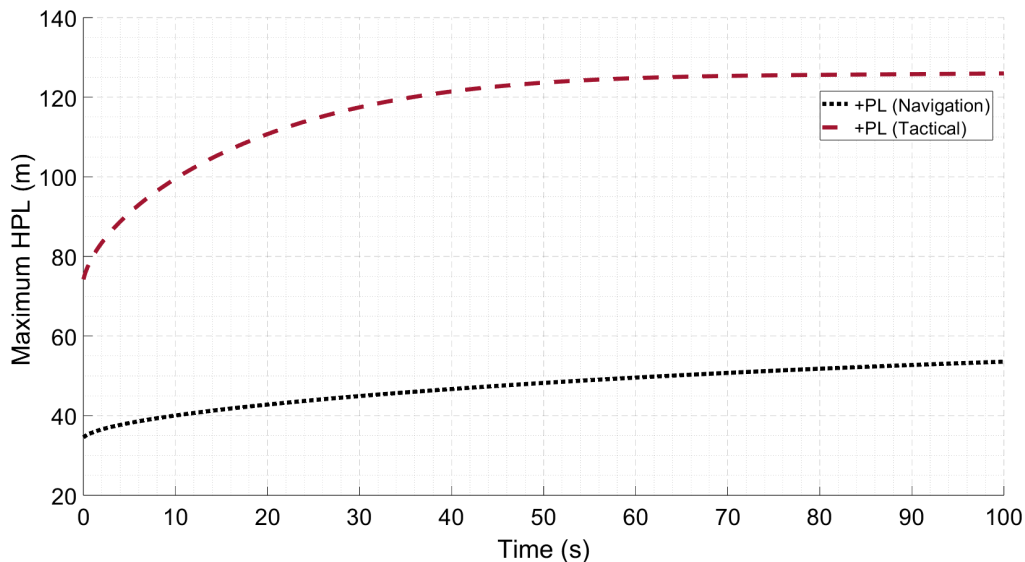


Figure 16: Maximum horizontal protection level (HPL) for navigation and tactical grade IMU.

V. CONCLUSION

As GNSS vulnerabilities continue to impact the aviation industry, there is increasing interest in developing APNT systems that can satisfy RNP 1 requirements. In this work, we develop a DME/INS-integrated KF-based APNT system that meets RNP 1 requirements for a representative trajectory over European airspace. Performance is evaluated for both a multi-DME KF and a

DME/INS KF system, with comparisons across various grades of IMU, including INS coasting behavior during DME outages. We present protection level results using a solution-separation-based FDE approach that satisfies the integrity requirements for RNP 1.

REFERENCES

- Berz, G., Vitan, V., and Skyrda, I. (2013). Can Current DME Support PBN Operations with Integrity? In *Proceedings of the 26th International Technical Meeting of the Satellite Division of The Institute of Navigation (ION GNSS+ 2013)*, pages 233–250.
- Berz, G. E. and Saini, L. (2022). Reengineering DME/N integrity to support PBN. In *International Flight Inspection Symposium*.
- Brown, R. and Hwang, P. (2012). *Introduction to Random Signals and Applied Kalman Filtering with Matlab Exercises*. John Wiley.
- EUROCAE WG-107 (1986). *ED-57 - MINIMUM PERFORMANCE SPECIFICATION FOR DISTANCE MEASURING EQUIPMENT (DME/N and DME/P)*. EUROCAE.
- Gebre-Egzabher, D., Powell, J., and Enge, P. (2000). A DME based area navigation systems for GPS/WAAS interference mitigation in general aviation applications. In *IEEE 2000. Position Location and Navigation Symposium (Cat. No.00CH37062)*, pages 74–81.
- Gordo, V. M., Paz, G. A., and San-Juan, J. (2019). DME multipath simulations as a critical enabler to support DME/DME RNP reversion. In *Proceedings of the 2019 International Technical Meeting of The Institute of Navigation*, pages 508–521.
- Gunning, K., Blanch, J., Walter, T., de Groot, L., and Norman, L. (2018). Design and evaluation of integrity algorithms for PPP in kinematic applications. In *Proceedings of the 31st International Technical Meeting of the Satellite Division of the Institute of Navigation (ION GNSS+ 2018)*, pages 1910 – 1939.
- Gunning, K., Blanch, J., Walter, T., de Groot, L., and Norman, L. (2019). Integrity for tightly coupled PPP and IMU. In *Proceedings of the 32nd International Technical Meeting of the Satellite Division of The Institute of Navigation (ION GNSS+ 2019)*, pages 3066–3078.
- International Civil Aviation Organization (2023). *Performance Based Navigation (PBN) Manual (Doc 9613)*. ICAO, 5th edition.
- Kelly, R. and Cusick, D. (1986). Distance measuring equipment and its evolving role in aviation. In *Advances in Electronics and Electron Physics*, volume 68, pages 1–243. Elsevier.
- Kerns, A. J., Shepard, D. P., Bhatti, J. A., and Humphreys, T. E. (2014). Unmanned aircraft capture and control via GPS spoofing. *Journal of Field Robotics*, 31(4):617–636.
- Kim, E. (2022). Development of highly accurate stretched-front-leg distance-measuring equipment and the testbed results. In *20th International Flight Inspection Symposium (IFIS)*.
- Kujur, B., Khanafseh, S., and Pervan, B. (2024). Optimal INS monitor for GNSS spoofer tracking error detection. *NAVIGATION*, 71(1).
- Latham, R. W. and Richards, P. T. (1977). A multi-DME/inertial system for aircraft positioning. *NAVIGATION*, 24(1):72–83.
- Lo, S., Chen, Y., Enge, P., Peterson, B., Erikson, R., and Lilley, R. (2013). Distance measuring equipment accuracy performance today and for future alternative position navigation and timing (APNT). In *Proceedings of the 26th International Technical Meeting of the Satellite Division of The Institute of Navigation (ION GNSS+ 2013)*, pages 711–721.
- Lo, S., Chen, Y., Segal, B., Peterson, B., Enge, P., Erikson, R., and Lilley, R. (2014). Containing a difficult target: Techniques for mitigating DME multipath to alternative position navigation and timing (APNT). In *Proceedings of the 2014 International Technical Meeting of The Institute of Navigation (ITM 2014)*, pages 413–423.
- Lo, S., Chen, Y.-H., Enge, P., Pelgrum, W., Li, K., Weida, G., and Soelter, A. (2020). Flight test of a pseudo-ranging signal compatible with existing distance measuring equipment (DME) ground stations. *NAVIGATION*, 67(3):567–582.
- Lo, S. and Enge, P. (2012a). Signal structure study for a passive ranging system using existing distance measuring equipment (DME). In *Proceedings of the 2012 International Technical Meeting of The Institute of Navigation*, pages 97–130.
- Lo, S. C. and Enge, P. (2012b). Assessing the capability of distance measuring equipment (DME) to support future air traffic capacity. *NAVIGATION*, 59(4):249–261.

- Lo, S. C., Enge, P. K., and Narins, M. J. (2015). Design of a passive ranging system using existing distance measuring equipment (DME) signals & transmitters. *NAVIGATION*, 62(2):131–149.
- Osechas, O., Narayanan, S., Zampieri, G., and Weaver, B. (2023). A distributed, collaborative strategy for in-situ monitoring of multipath errors. In *Proceedings of the 2023 International Technical Meeting of The Institute of Navigation*, pages 172–178.
- Osechas, O., Zampieri, G., and Schneckenburger, N. (2020). A new error model for terrestrial multipath. In *Proceedings of the 33rd International Technical Meeting of the Satellite Division of The Institute of Navigation (ION GNSS+ 2020)*, pages 99–113.
- Osechas, O., Zampieri, G., Weaver, B., Felux, M., Dehaynain, C., Berz, G., Vitan, V., and Scaramuzza, M. (2022). A standardizable framework enabling DME/DME to support RNP. In *Proceedings of the 35th International Technical Meeting of the Satellite Division of The Institute of Navigation (ION GNSS+ 2022)*, page 2020–2024.
- Pelgrum, W. and Li, K. (2015). An investigation on the contributing factors of enhanced DME ranging errors. In *Proceedings of the 28th International Technical Meeting of the Satellite Division of The Institute of Navigation (ION GNSS+ 2015)*, pages 1333–1380.
- RTCA SC-159 (2020). DO-384, Minimum Operational Performance Standards MOPS for GNSS Aided Inertial Systems. Technical report, RTCA.
- RTCA-SC-227 (2014). RTCA DO-236C, Minimum Aviation System Performance Standards: Required Navigation Performance for Area Navigation. Technical report, RTCA.
- RTCA SC-227 (2015). DO-283B - Minimum operational performance standards: Required navigation performance for area navigation.
- RTCA SC-227 (2025a). DO-236E - Minimum Aviation System Performance Standards: Required Navigation Performance for Area Navigation. Technical report, RTCA.
- RTCA SC-227 (2025b). DO-283C - Minimum Operational Performance Standards for Required Navigation Performance for Area Navigation. Technical report, RTCA.
- Strecha, P., Makula, P., and Dycka, P. (2018). DME/DME/ADAHRS positioning using a particle filter. In *2018 IEEE/AIAA 37th Digital Avionics Systems Conference (DASC)*, pages 1–7.
- Tanil, C., Khanafseh, S., Joerger, M., Kujur, B., Kruger, B., de Groot, L., and Pervan, B. (2019). Optimal INS/GNSS coupling for autonomous car positioning integrity. In *Proceedings of the 32nd International Technical Meeting of the Satellite Division of The Institute of Navigation (ION GNSS+ 2019)*, pages 3123–3140.
- Tripathi, V. and Caizzone, S. (2024). Power absorbing structure for multipath suppression in DME applications. In *Proceedings of the 2024 International Technical Meeting of The Institute of Navigation*, pages 998–1006.
- Vitan, V., Berz, G., Osechas, O., Scaramuzza, M., and Zampieri, G. (2022). Quantifying DME-N multipath in the context of PBN. In *Proceedings of the International Flight Inspection Symposium (IFIS)*. Durban, ZA.
- Vitan, V., Berz, G., and Solomina, N. (2015). Assessment of current DME performance and the potential to support a future A-PNT solution. In *2015 IEEE/AIAA 34th Digital Avionics Systems Conference (DASC)*, pages 2A2–1–2A2–18.
- Vitan, V. and Theißen, K. (2016). DME SiS performance and DME/DME positioning using in-flight recorded data. In *19th International Flight Inspection Symposium (IFIS)*, pages 2A2–1–2A2–18.
- Zampieri, G., Weaver, B., Osechas, O., Berz, G., and Meurer, M. (2021). Range-domain fault monitoring for terrestrial ranging systems. In *Proceedings of the 34th International Technical Meeting of the Satellite Division of The Institute of Navigation (ION GNSS+ 2021)*, pages 2242–2252.

APPENDIX

A. Multi-DME KF model

a) Process Model

We consider an example straight level flight scenario where an aircraft starts from a given location traveling at cruising constant speed along a given direction (Brown and Hwang (2012)). It utilizes multiple DME for ranging and a barometric altimeter for altitude measurements. The aircraft is assumed to experience small random accelerations in all three-dimensional directions that cause perturbations in aircraft velocity and position.

An East-North-Up reference navigation frame is assumed to be fixed at the starting location of the aircraft. We first start with aircraft position x, y, z , and velocity V_x, V_y, V_z states whose dynamics can be written as

$$\begin{bmatrix} \dot{x} \\ \dot{y} \\ \dot{z} \\ \dot{V}_x \\ \dot{V}_y \\ \dot{V}_z \end{bmatrix} = \begin{bmatrix} V_x \\ V_y \\ V_z \\ u_x \\ u_y \\ u_z \end{bmatrix} \quad (9)$$

where u_x, u_y , and u_z are the random accelerations in the three position directions. These random accelerations are modelled to have zero-mean Gaussian distribution given as

$$u_x \sim \mathcal{N}(0, \sigma_{a_x}^2), \quad (10)$$

$$u_y \sim \mathcal{N}(0, \sigma_{a_y}^2), \quad (11)$$

$$u_z \sim \mathcal{N}(0, \sigma_{a_z}^2). \quad (12)$$

We can write the above continuous dynamics equations in state-space model form

$$\dot{\mathbf{x}} = \mathbf{F} \mathbf{x} + \mathbf{G} \mathbf{w}, \quad (13)$$

where the process model matrix \mathbf{F} is given by

$$\mathbf{F} = \begin{bmatrix} 0 & 0 & 0 & 1 & 0 & 0 \\ 0 & 0 & 0 & 0 & 1 & 0 \\ 0 & 0 & 0 & 0 & 0 & 1 \\ 0 & 0 & 0 & 0 & 0 & 0 \\ 0 & 0 & 0 & 0 & 0 & 0 \\ 0 & 0 & 0 & 0 & 0 & 0 \end{bmatrix} \quad (14)$$

the process noise model matrix \mathbf{G} as identity matrix, the process noise vector w as

$$\mathbf{w} = \begin{bmatrix} 0 \\ 0 \\ 0 \\ u_x \\ u_y \\ u_z \end{bmatrix} \quad (15)$$

and the state vector as

$$\mathbf{x} = \begin{bmatrix} x \\ y \\ z \\ V_x \\ V_y \\ V_z \end{bmatrix} \quad (16)$$

This continuous-time equation can be discretized to yield the discrete-time process model as follows:

$$\mathbf{x}_{k+1} = \mathbf{\Phi}_k \mathbf{x}_k + \mathbf{\Gamma}_{w_k} \mathbf{w}_k, \quad (17)$$

where $\mathbf{\Phi}_k$ is the state transition matrix, $\mathbf{\Gamma}_{w_k}$ the discrete-time process noise model matrix, with an associated process noise covariance matrix \mathbf{Q}_k . These matrices characterize the evolution of the state vector and its uncertainty across discrete time steps in the navigation filter.

b) *Measurement Model*

The barometric altimeter sensor measurement h_{baro} can be modelled as true measurement h with an additive constant bias Δh and white Gaussian noise v_{baro} given as

$$h_{baro} = h + \Delta h + v_{baro}. \quad (18)$$

The constant bias and noise are distributed Normally with zero-mean as

$$\Delta h \sim \mathcal{N}(0, \sigma_{baro\ bias}^2), \quad (19)$$

$$v_{baro} \sim \mathcal{N}(0, \sigma_{baro}^2), \quad (20)$$

The constant bias Δh can be augmented as a state and added to the state dynamics as

$$\begin{bmatrix} \dot{x} \\ \dot{y} \\ \dot{z} \\ \dot{V}_x \\ \dot{V}_y \\ \dot{V}_z \\ \dot{\Delta h} \end{bmatrix} = \begin{bmatrix} V_x \\ V_y \\ V_z \\ u_x \\ u_y \\ u_z \\ 0 \end{bmatrix} \quad (21)$$

with the updated state vector as

$$\mathbf{x} = \begin{bmatrix} x \\ y \\ z \\ V_x \\ V_y \\ V_z \\ \Delta h \end{bmatrix} \quad (22)$$

The process model matrix and the process noise vector are augmented to accommodate the new baro bias state.

The aircraft utilizes multiple DME measurements simultaneously along with barometric altimeter sensor. The DME slant range measurement ρ_{dme} is modelled as true slant range r of DME from aircraft with additive white Gaussian noise v_{dme} , represented for j^{th} DME as

$$\rho_{dme\ j} = r_j + v_{dme\ j}. \quad (23)$$

The noise on DME measurements has zero-mean Gaussian distribution as

$$v_{dme\ j} \sim \mathcal{N}(0, \sigma_{dme\ j}^2). \quad (24)$$

For n DME measurements and one barometric altimeter measurement, we can write the measurement vector \mathbf{z} as

$$\mathbf{z} = \begin{bmatrix} \rho_{dme\ 1} \\ \rho_{dme\ 2} \\ \vdots \\ \rho_{dme\ n-1} \\ \rho_{dme\ n} \\ h_{baro} \end{bmatrix} \quad (25)$$

The non-linear measurement equation is represented as

$$\mathbf{z} = h(\mathbf{x}) + \mathbf{v}, \quad (26)$$

where (Note that the subscript ‘a’ is used for aircraft)

$$h(\mathbf{x}) = \begin{bmatrix} \sqrt{(x_{dme\ 1} - x_a)^2 + (y_{dme\ 1} - y_a)^2 + (z_{dme\ 1} - z_a)^2} \\ \sqrt{(x_{dme\ 2} - x_a)^2 + (y_{dme\ 2} - y_a)^2 + (z_{dme\ 2} - z_a)^2} \\ \vdots \\ \sqrt{(x_{dme\ n-1} - x_a)^2 + (y_{dme\ n-1} - y_a)^2 + (z_{dme\ n-1} - z_a)^2} \\ \sqrt{(x_{dme\ n} - x_a)^2 + (y_{dme\ n} - y_a)^2 + (z_{dme\ n} - z_a)^2} \\ z_a + \Delta h \end{bmatrix} \quad (27)$$

and measurement noise vector \mathbf{v} as.

$$\mathbf{v} = \begin{bmatrix} v_{dme\ 1} \\ v_{dme\ 2} \\ \vdots \\ v_{dme\ n-1} \\ v_{dme\ n} \\ v_{baro} \end{bmatrix} \quad (28)$$

The measurement equation is linearized and can be written in standard form as

$$\mathbf{z} = \mathbf{H}\mathbf{x} + \mathbf{v}, \quad (29)$$

where the observation matrix \mathbf{H} is

$$\mathbf{H} = \begin{bmatrix} -\cos(\beta_1)\cos(\theta_1) & -\cos(\beta_1)\sin(\theta_1) & \sin(\beta_1) & 0 & 0 & 0 & 0 \\ -\cos(\beta_2)\cos(\theta_2) & -\cos(\beta_2)\sin(\theta_2) & \sin(\beta_2) & 0 & 0 & 0 & 0 \\ \vdots & \vdots & \vdots & \vdots & \vdots & \vdots & \vdots \\ -\cos(\beta_{n-1})\cos(\theta_{n-1}) & -\cos(\beta_{n-1})\sin(\theta_{n-1}) & \sin(\beta_{n-1}) & 0 & 0 & 0 & 0 \\ -\cos(\beta_n)\cos(\theta_n) & -\cos(\beta_n)\sin(\theta_n) & \sin(\beta_n) & 0 & 0 & 0 & 0 \\ 0 & 0 & 1 & 0 & 0 & 0 & 1 \end{bmatrix} \quad (30)$$

where, β is the elevation angle of DME range with respect to navigation frame XY plane as illustrated in Figure 3, and θ is the the DME range vector makes with the reference X-axis of navigation frame as illustrated in Figure 4. The measurement noise matrix is zero-mean Normally distributed

$$\mathbf{v} \sim \mathcal{N}(0, \mathbf{V}), \quad (31)$$

where \mathbf{V} is the measurement noise covariance matrix given as

$$\mathbf{V} = \begin{bmatrix} \sigma_{dme\ 1}^2 & 0 & 0 & 0 & 0 & 0 & 0 \\ 0 & \sigma_{dme\ 2}^2 & 0 & 0 & 0 & 0 & 0 \\ 0 & 0 & \sigma_{dme\ 3}^2 & 0 & 0 & 0 & 0 \\ \vdots & \vdots & \vdots & \ddots & \vdots & \vdots & \vdots \\ 0 & 0 & 0 & 0 & \sigma_{dme\ n-1}^2 & 0 & 0 \\ 0 & 0 & 0 & 0 & 0 & \sigma_{dme\ n}^2 & 0 \\ 0 & 0 & 0 & 0 & 0 & 0 & \sigma_{baro}^2 \end{bmatrix} \quad (32)$$

B. DME/INS KF model

a) Process Model

An East-North-Up reference navigation frame is assumed to be fixed at the starting location of the aircraft. Based on IMU measurements, the INS provides the navigation state vector, which includes the aircraft’s position vector \mathbf{r} with components x , y , z , velocity vector \mathbf{v} with components u , v , w , and attitude ϕ , θ , ψ (Euler angles):

$$\mathbf{x}_{A/C} = [x \ y \ z \ u \ v \ w \ \phi \ \theta \ \psi]^T \quad (33)$$

An IMU comprises tri-axis accelerometers and gyroscopes that measure specific force and body angular rates. In an INS, the accelerometer measurements are integrated once to derive velocity and then again to obtain position, while attitude is derived by integrating the gyroscope outputs. However, these measurements are subject to errors, such as biases and noise, which cause the state estimates to drift over time. In a tightly coupled architecture, a KF fuses raw GNSS code and carrier-phase measurements to estimate and correct INS errors, thereby producing an integrated navigation solution.

A scalar IMU measurement, denoted \tilde{u} , is affected by errors such as time-dependent biases and noise. It is therefore modeled as the “true” value u^* corrupted by a constant bias b_c , a slowly varying time-dependent bias component b , and additive white Gaussian noise (WGN) η_u , as shown in Equation (34). The constant bias is typically characterized by bias repeatability, while the WGN component η_u is commonly specified using the velocity random walk (VRW) for accelerometers and angular random walk (ARW) for gyroscopes.

$$\tilde{u} = u^* + b_c + b + \eta_u \quad (34)$$

The time-dependent bias component b is modeled as a first-order Gauss–Markov random process (GMRP) with time constant τ_b and a driving WGN term v_b . This driving noise is derived from the IMU’s bias instability specifications.

$$\dot{b} = -\frac{1}{\tau_b}b + v_b \quad (35)$$

The bias dynamics are incorporated into the process model by augmenting the aircraft state vector with the bias states, denoted \mathbf{x}_{bias} . For each of the three IMU axes, the bias states corresponding to both acceleration and angular rate measurements are represented in Equation (36).

$$\mathbf{x}_{bias} = [b_{a_x} \quad b_{a_y} \quad b_{a_z} \quad b_{\omega_x} \quad b_{\omega_y} \quad b_{\omega_z}]^T \quad (36)$$

Together, Equations (33) and (36) define the complete set of nominal states propagated to compute the INS navigation solution.

Detailed INS mechanization equations can be found in (Brown and Hwang (2012)). The continuous-time differential equations governing the system dynamics can be expressed in state-space form as follows:

$$\dot{\mathbf{x}} = \mathbf{F}\mathbf{x} + \mathbf{G}\mathbf{w} \quad (37)$$

where \mathbf{x} is the state vector, \mathbf{F} is the INS mechanization matrix augmented with bias dynamics, \mathbf{G} is the continuous-time process noise model matrix, and \mathbf{w} represents the additive white process noise.

b) Measurement Model

The measurement model for the DME/INS integration follows the same architecture as described in Appendix .A. Multiple DME units and a barometric altimeter are used as sensors in the measurement model of the DME/INS system.

The barometric altimeter sensor measurement model is described using Equations (18), (19), and (20).

The constant bias Δh as an additional state is incorporated into the overall state vector \mathbf{x}

$$\mathbf{x} = [\mathbf{x}_{A/C} \quad \mathbf{x}_{bias} \quad \Delta h]^T \quad (38)$$

The aircraft utilizes multiple DME measurements simultaneously, along with a barometric altimeter sensor. The DME measurement model is described using Equations (23) and (24).

For n DME measurements and one barometric altimeter measurement, the measurement vector \mathbf{z} can be expressed using Equation (25).

The non-linear measurement equation is represented using Equation (26), (27), and (28).

The measurement equation is linearized and expressed in the standard form as:

$$\mathbf{z} = \mathbf{H}\mathbf{x} + \mathbf{v}. \quad (39)$$

The observation matrix \mathbf{H} accommodates all the states and is represented as the Jacobian of the measurement function with

respect to the state vector, evaluated at the current state estimate:

$$\mathbf{H} = \begin{bmatrix} -\cos(\beta_1)\cos(\theta_1) & -\cos(\beta_1)\sin(\theta_1) & \sin(\beta_1) & \mathbf{0}_{[1 \times 12]} & 0 \\ -\cos(\beta_2)\cos(\theta_2) & -\cos(\beta_2)\sin(\theta_2) & \sin(\beta_2) & \mathbf{0}_{[1 \times 12]} & 0 \\ \vdots & \vdots & \vdots & \vdots & \vdots \\ -\cos(\beta_{n-1})\cos(\theta_{n-1}) & -\cos(\beta_{n-1})\sin(\theta_{n-1}) & \sin(\beta_{n-1}) & \mathbf{0}_{[1 \times 12]} & 0 \\ -\cos(\beta_n)\cos(\theta_n) & -\cos(\beta_n)\sin(\theta_n) & \sin(\beta_n) & \mathbf{0}_{[1 \times 12]} & 0 \\ 0 & 0 & 1 & \mathbf{0}_{[1 \times 12]} & 1 \end{bmatrix} \quad (40)$$

where, β denotes the elevation angle of the DME range vector with respect to the XY-plane of the navigation frame, as illustrated in Figure 3; and θ denotes the angle between the DME range vector and the X-axis of the navigation frame, as shown in Figure 4. The measurement noise is modeled as a zero-mean Gaussian distribution given in Equation (31) and the measurement noise covariance matrix in Equation (32).

C. Multi-DME KF vs DME/INS KF

The covariance results for the multi-DME-only KF presented below were computed using an acceleration noise standard deviation of $0.6g$ (6 m/s^2).

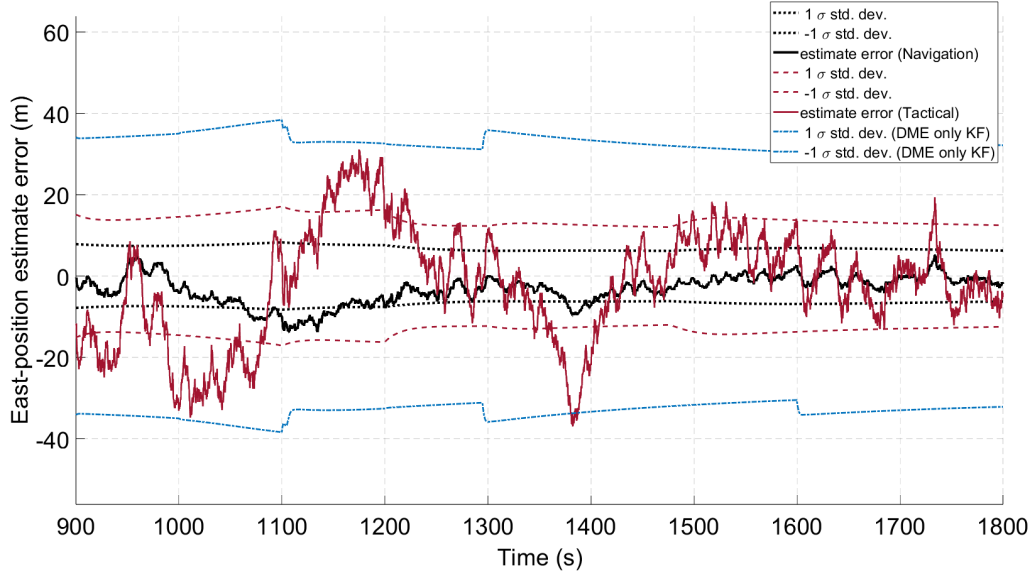


Figure 17: Illustration of multi-DME KF vs DME/INS KF East position estimate error and covariance.

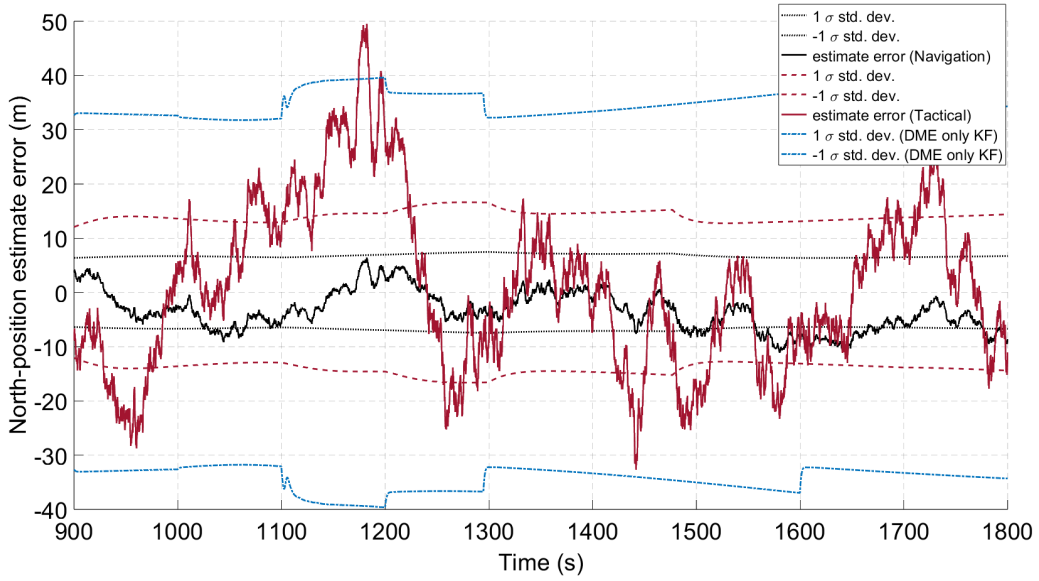


Figure 18: Illustration of multi-DME KF vs DME/INS KF North position estimate error and covariance.

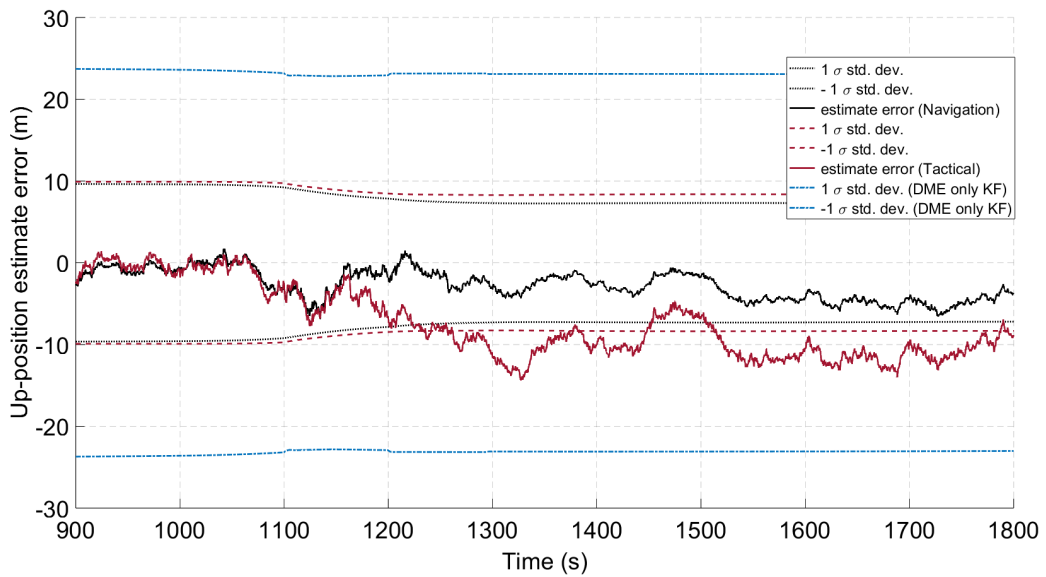


Figure 19: Illustration of multi-DME KF vs DME/INS KF Up position estimate error and covariance.

D. IMU specifications

Table 4: Specifications for different IMU grades

Parameter	Navigation	Low tactical	Unit
Velocity random walk	1.43×10^{-2}	7×10^{-2}	m/s/ \sqrt{h}
Accelerometer bias instability	1×10^{-2}	4×10^{-2}	mg
Accelerometer bias repeatability	2.5×10^{-2}	0.75	mg
Accelerometer bias time constant	3600	3600	s
Angular random walk	1×10^{-3}	0.15	deg/ \sqrt{h}
Gyroscope bias instability	3.5×10^{-3}	0.3	deg/h
Gyroscope bias repeatability	3×10^{-3}	4	deg/h
Gyroscope time constant	3600	3600	s